Corrosion Science 259 (2026) 113496

Contents lists available at ScienceDirect

Corrosion Science

journal homepage: www.elsevier.com/locate/corsci

Understanding hydrogen diffusion and trapping in overaged 7xxx series Al alloys using a reliable electrochemical hydrogen permeation method

Oliver Beyss [a], Chijioke Kenneth Akuata [a,b], Laura Kopruch [a], Daniela Zander [a,b,*]

[a] Chair of Corrosion and Corrosion Protection, Foundry Institute, Division of Materials Science and Engineering, RWTH Aachen University, Intzestraße 5, 52072 Aachen, Germany

[b] Deutsches Zentrum für Luft- und Raumfahrt, German Aerospace Center, Institute for Frontier Materials on Earth and in Space, Linder Höhe, 51147 Cologne, Germany

ARTICLE INFO

Keywords:
Hydrogen permeation
7xxx aluminum alloys
Hydrogen diffusion
Hydrogen trapping

ABSTRACT

The diffusion and trapping of H in overaged commercial 7xxx series alloys of the second and third generation is first studied using an enhanced electrochemical permeation method involving sputter etching of the native oxide and hydrogen charging by alkaline corrosion at the open circuit potential. Proof of concept is provided demonstrating remarkable experimental reproducibility and addressing common experimental errors, such as native oxide films, localized corrosion and buildup of corrosion products. A commercial second and third generation 7xxx series alloy exhibit effective H diffusion coefficients of $1.6 \pm 0.7 \times 10^{-10}$ cm^2/s and $3.7 \pm 0.3 \times 10^{-10}$ cm^2/s, respectively. The different H diffusivities were explained by extensive H trapping in coarse intermetallic Al_7Cu_2Fe and S-phase particles, alongside potential trapping at the interface of quench-induced grain-boundary precipitates with lower Zn content.

1. Introduction

With an ever-growing demand for lightweight solutions, increased sustainability, and green hydrogen technologies in the mobility sector, Al alloys face an increased requirement for mechanical strength, fracture toughness and corrosion resistance, as well as increased exposure to hydrogen in service [1–5]. Even though these alloys are tried and trusted for decades in many applications from automotive [6,7] to aviation [2,8] and space [9,10], the interactions of hydrogen with the metallic material are still an active field of research. Because of its volatile nature and its low atomic number, measuring hydrogen is a challenging task for most analytical methods typically used in materials science. However, numerous research papers on this topic are published every year because of the recent development of more sophisticated analytic [11–14] and computational approaches [15–18]. Besides a more novel interest in the suitability of Al alloys for long-term usage in hydrogen storage facilities [19,20], a lot of research in the past focused on the understanding of stress corrosion cracking (SCC) or hydrogen environmentally assisted cracking (HEAC) of 7xxx series alloys frequently used in aerospace applications [21–25]. Crack formation and propagation in these alloys was often found to be governed by hydrogen embrittlement [22,23,25,26]. Despite experimental evidence for hydrogen embrittlement, however, the exact mechanisms of hydrogen absorption and transport during cracking are typically not tangible. In addition, hydrogen diffusivity data reported in the literature does not allow for reliable conclusions with hydrogen diffusion coefficients covering a range of over 17 orders of magnitude, even for pure Al [27,28].

Characterization of hydrogen diffusion and trapping in metallic materials is often performed by thermal desorption [29–32] or hydrogen permeation experiments in a gaseous [33,34] or electrochemical environment [35–37]. In the latter case, a Devanathan-Stachurski cell setup is typically used [35]. In this setup, a thin membrane of the sample material is clamped between two cells, where one side is exposed to a hydrogen charging environment, typically cathodic polarization, and the other side is anodically polarized to oxidize and quantify hydrogen using the oxidation current. From the time lag between the start of hydrogen charging and the detection of a steady state on the exit side, information about the diffusion and trapping of H in the membrane can be deduced [35]. Electrochemical hydrogen permeation experiments have already been used for a wide range of metallic materials, such as Fe-based materials [38,39], Al [40–42], Ni [43] and Fe-Al intermetallics [44]. The standard ASTM G148, dedicated to this method, considers it

* Corresponding author at: Chair of Corrosion and Corrosion Protection, Foundry Institute, Division of Materials Science and Engineering, RWTH Aachen University, Intzestraße 5, 52072 Aachen, Germany.

E-mail addresses: o.beyss@gi.rwth-aachen.de (O. Beyss), k.akuata@gi.rwth-aachen.de (C.K. Akuata), l.kopruch@gi.rwth-aachen.de (L. Kopruch), d.zander@gi.rwth-aachen.de (D. Zander).

https://doi.org/10.1016/j.corsci.2025.113496
Received 17 September 2025; Received in revised form 28 October 2025; Accepted 20 November 2025
Available online 21 November 2025

applicable "in principle to all metals and alloys, which have a high solubility for hydrogen, and for which the hydrogen permeation is measurable" [45]. While this statement is vague and ambiguous in the case of Al with its poor H solubility [28], several researchers succeeded to measure hydrogen permeation using this method. Danielson summarized some past attempts on electrochemical permeation of Al alloys in 2002 [46] and identified some common problems: The reproducibility of hydrogen permeation data for Al is often poor and the ubiquitous oxide film on Al acts as a strong diffusion barrier [47,48]. Thus, Braun et al. used ion sputtering to remove the oxide film and then captured the fresh surface under a Pd film [49,50]. Even though the exact procedure was not described and the effect of the ion etching was not demonstrated, the authors claimed a higher reliability of their diffusion data. Another factor exacerbating the reliability of permeation data is the strong dependence on microstructural trap sites, i.e. crystal defects like vacancies and dislocations, grain boundaries, interfaces and constituent phases that can bind hydrogen to various extents [29,30]. Depending on the binding energy for hydrogen, the different microstructural features are considered reversible or irreversible trap sites [36]. If the material is first charged with hydrogen, the apparent or effective hydrogen diffusion coefficient ($D_{H,eff}$) is measured. $D_{H,eff}$ describes the hydrogen mobility affected by reversible and irreversible trap sites in the material. For most technical applications involving SCC or HEAC, where the material fails well before global H saturation of the material is achieved, this scenario applies. Thermomechanical processing and tempering of precipitation hardened Al alloys can have a strong effect on the type and density of microstructural trap sites, and therefore also on the measured $D_{H,eff}$ [51,52]. Thus, it is not possible to compare hydrogen permeation data in the literature without detailed knowledge of the processing history and the resulting microstructure. A modified method for hydrogen permeation measurements on Al alloys was first described by Hebert et al. [53] and further developed by Scully et al. [54,55], where the cathodic hydrogen charging is replaced by free corrosion at the open circuit potential in an alkaline environment and anodic oxidation of hydrogen is replaced by monitoring of the open-circuit potential transients of a thin Pd coating. This approach immediately mitigated the error induced by the oxide film on the charging side, and simultaneously allowed for very sensitive detection of H using the strong effect of Pd/ Pd hydride conversion on its electrochemical potential [56,57]. Implementing a cleaning procedure for reproducible Pd surfaces [58] and sample thickness variation [54,55] to verify bulk diffusion control according to Fick's laws enhanced the reliability of the permeation data. This method was successfully applied to pure Al and 5xxx series alloys [54,55]. The effect of the native oxide under the Pd coating however, was not addressed in these works.

The aim of this work is to study the hydrogen diffusion and trapping in commercial 7xxx series Al alloys using a reliable practice for electrochemical permeation measurements. By building on the knowledge from the literature and providing proof of concept for the elimination of common experimental errors, we present a rigorous and approachable method for characterizing hydrogen diffusion and trapping in Al alloys. Together with recent work on lab-cast alloys from Akuata et al. [59], we present the first successful application of this method for technologically highly relevant 7xxx series alloys in an overaged temper and demonstrate the potential synergy of permeation experiments and complementary analytical and simulation data for enhancing the understanding the role of hydrogen diffusion during SCC and HEAC.

2. Methodology

2.1. Material and alloy membrane preparation

Two commercial Al-Zn-Mg-Cu alloys in an overaged T7651 condition were investigated in this study. The chemical compositions are given in Table 1. The higher Zn alloy A belongs to the "new generation" alloys with higher Zn/Mg ratio and is prone to HEAC in humid air, while alloy B is an established alloy with lower Zn content, that is not susceptible to HEAC in this condition [25]. The material was provided as a thick plate (140 mm) and samples were taken from the t/4 position within the plate to avoid effects of segregation in thickness direction (ST) on the microstructure and the permeation results. 15 × 15 mm samples were cut in such a way, that the hydrogen diffusion in the permeation experiment occurred in the ST direction of the plate. This was done to prevent coarse intermetallic particles, that are elongated in the rolling direction of the plate (L), from penetrating the full final thickness of the alloy membrane. Iterative grinding up to 4000 grit under ethanol and thickness measurements in 5 spots were performed to achieve a uniform (deviation within a sample <3 μm) final thickness of the alloy membranes between 40 and 120 μm. Additionally, some experiments were performed on commercially pure Al foil (Carl Roth GmbH) with a thickness of 30 μm.

Table 1
Chemical composition of investigated alloys.

Composition (wt%)	Al	Zn	Mg	Cu	Zr	Ti	Fe	Si
Alloy A	bal.	7.3	1.5	1.7	0.11	0.02	0.03	0.03
Alloy B	bal.	6.2	2.1	2.1	0.11	0.03	0.06	0.03

The thinned membranes and foil samples were then individually introduced into a vacuum chamber ($p_{Base}=10^{-7}$ mbar) for plasma etching and coating. Plasma etching was performed on one side of the sample in a 1 Pa Ar atmosphere using a 250 kHz pulsed DC generator at 50 W for 3 min. These parameters were deemed to be sufficient for removal of the nm thin native oxide layer. For some pure Al foil samples, this etching step was skipped. Subsequent to plasma etching, the gas flow was quickly regulated to achieve 0.5 Pa Ar and DC magnetron sputtering from a Pd target ($\varnothing = 5$ cm) was started to cap the reactive Al surface under a Pd coating before the oxide film can re-form with O in the residual gas of the vacuum chamber. This switching process took no more than 5 s. The Pd deposition was carried out at 50 W for another 3 min. This led to a coating thickness of around 50 nm Pd calibrated by cross section SEM (see Figure A 1). A schematic of the full preparation route for the permeation samples is displayed in Fig. 1.

2.2. Interface analysis for Pd coatings

X-ray photoelectron spectroscopy in combination with Ar^+ ion sputtering was used to investigate the presence of oxides at the alloy/Pd interface. Measurements were performed in a Kratos Axis Supra instrument using a monochromatic Al Kα X-ray source ($h\nu$=1486.6 eV) and a hemispherical analyzer. The base pressure of the instrument was 10^{-9} mbar. Survey spectra and high-resolution scans were recorded at a pass energy of 160 eV and 20 eV, respectively. A step size of 0.25 eV was used for overview survey spectra, while high-resolution spectra were measured with a step size of 0.1 eV. Iterative ion etching steps using a kinetic energy of 500 eV for 30 s gradually removed the Pd coating until the expected Al 2p and Al 2 s signals of the substrate (among other alloying element peaks) appeared in the spectra. The presence of both of the substrate signal and a strong Pd signal allowed for the observation of the buried Al alloy/coating interface in the as deposited state. Kratos' ESCApe software was used for data evaluation.

2.3. Hydrogen permeation tests

Hydrogen permeation tests were carried out in a commercially available electrochemical double cell (IPS Elektroniklabor GmbH) using standard calomel reference electrodes (SCE) in saturated KCl and counter electrodes made from platinized titanium. A sketch of the experimental setup is given in Fig. 2. The cells were temperature controlled to 25°C using a thermostat for all experiments. The membrane was clamped between the cells with the Pd coated side facing the H detection cell and then connected to two Gamry Interface 1010

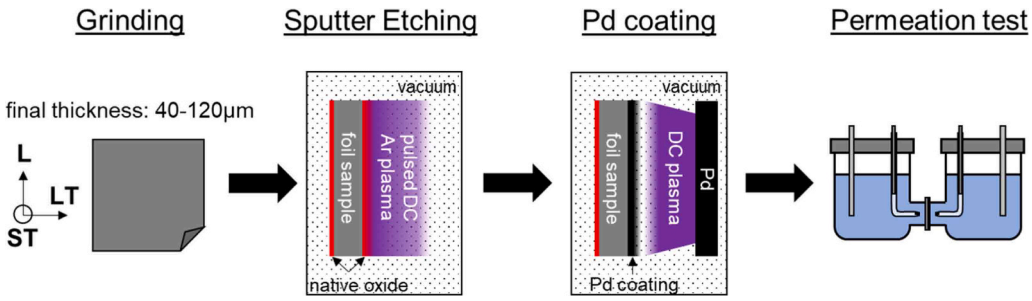

Fig. 1. Preparation routine for the hydrogen permeation samples.

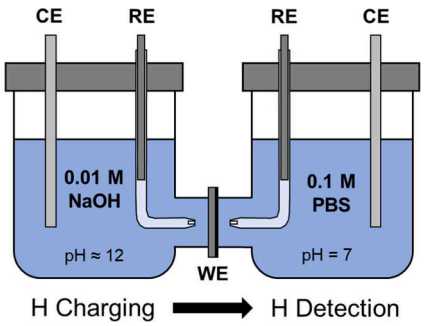

Fig. 2. Sketch of the electrochemical permeation setup used in this study.

potentiostats. The H detection cell was then filled with a naturally aerated 0.1 M NaH_2PO_4/Na_2HPO_4 phosphate buffer solution (PBS) with pH= 7 and an electrochemical cleaning procedure involving cyclic voltammetry and applying anodic and cathodic potentials to the Pd coating was carried out to ensure a clean Pd surface and reproducible OCP values. The parameters of this procedure were adapted from the literature [53,58]. Once the Pd potential stabilized at around 0.28 V_{SCE}, which is close to the Nernst potential of the Pd/PdO transition [60], the H charging cell was filled with naturally aerated 0.01 M NaOH solution (pH≈12). This marked the starting point of the permeation experiment and free corrosion at the entry side of the alloy membrane was initiated. The corrosive attack both dissolved the native oxide, that was still present on this side, and also generated high fugacity atomic hydrogen to absorb into and permeate through the alloy membrane. The OCP of both the charging and detection side was monitored until a rapid transient in the Pd potential to a plateau around −600 to −800 mV is observed, indicating the formation of PdH_x caused by the permeation of H atoms. According to the time lag approach from the literature, $t_{0.63}$, the time at which 63 % of the transient have passed, was considered for the calculation of the effective hydrogen diffusion coefficient $D_{H,eff}$ [35].

The corrosion rate on the H charging side of alloy membranes was determined by immersing samples of 15x15x2 mm in the 0.01 M NaOH charging solution and determining the mass loss at several time steps (6 h, 24 h, 48 h, 96 h and 168 h), corresponding to the experiment times in the hydrogen permeation test. To accurately determine the mass loss, the corroded samples were etched in conc. HNO_3 for 1 min to remove corrosion products from the surface and subsequently cleaned with distilled water and ethanol and then dried [61]. By converting the mass loss to thickness reduction, this procedure allowed for the determination of the time-dependent corrosion rate of the permeation foils in the experiment. Eq. 1 was used for the calculation of the corrosion rate:

$$CR = \Delta m/\rho A t, \quad (1)$$

where CR, Δm, ρ, A and t are the corrosion rate, mass loss, density, corroded area and time, respectively. Knowledge of the time dependent corrosion rate is needed to determine $D_{H,eff}$ with a moving corrosion front. The thickness reduction at any given time could be calculated by integration of the corrosion rate from t = 0 to the time of interest. The corrected membrane thickness L_{corr} for the permeation experiment was then determined by taking the average of the initial membrane thickness and the thickness at which $t_{0.63}$ is reached. Determination of $D_{H,eff}$ was subsequently carried out with Eq. (2) according to Fick's laws of diffusion [35,36]

$$D_{H,eff} = L_{corr}^2/6t_{0.63}, \quad (2)$$

Where multiple experiments on the same material could be considered by plotting $L_{corr}^2/6$ versus the permeation times. An average $D_{H,eff}$ can then be determined from the slope of a linear regression line through origin.

2.4. Microstructural characterization

Microstructural analysis of the commercial alloy material was carried out by both SEM and TEM to elucidate the potential role of microstructural features on the H diffusion and trapping behavior. EDX spectra and backscatter electron images were recorded using a Zeiss Supra 55 VP, equipped with an Oxford Instruments EDX and EBSD detector to characterize and quantify the area fraction of coarse intermetallic particles. Quantification of the area fraction of bright Cu containing particles (Al_7Cu_2Fe, Al_2CuMg) was carried out in ImageJ using 1,000x magnification and a minimum of 10 BSE images per alloy.

For the characterization of grain boundary precipitates TEM lamellae were prepared from polished samples, where a region of interest was marked and mapped using EBSD to identify high angle grain boundaries. The lift-out was then performed in a Thermo Scientific Helios 5 Hydra UX DualBeam PFIB-SEM Xe^+ plasma focused ion beam (PFIB). After the lift out, the lamellae were attached to a Mo grid, thinned and transferred to a JEOL JEM-F200 STEM with a GATAN OneView high-resolution camera and an Oxford instruments EDX detector. The grain boundary η-$Mg(Zn,Cu,Al)_2$ precipitates and their chemical composition were then characterized by STEM imaging and EDX analysis at 200 kV.

3. Results

3.1. Interface analysis of the Pd coated samples

XPS analysis of the Al alloy/Pd interface was used to verify the effectiveness of the sputter etching step for the oxide layer removal. The results of the interfacial analysis are displayed in Fig. 3. The survey scans in Fig. 3a) show clear signals from the Pd 3d, 3p, and 3 s orbitals of the Pd coating. In the as deposited state, a C1s peak can be observed, that is a result of adventitious carbon from the atmosphere. In the etched state, this C signal disappears and the Pd signal becomes slightly stronger, enhancing smaller peaks of the Pd 4 s and 4p orbitals. Approaching the Al alloy/Pd interface, those features become intertwined with the photoelectron peaks from the Al-Zn-Mg-Cu alloy substrate, namely Al 2p and 2 s, Cu 2p and Zn 2p at higher binding energies. Some Ar^+ ion implantation is also evident from the arising Ar 2p peak. The high-resolution spectra of the Al 2p region at this interface and a reference

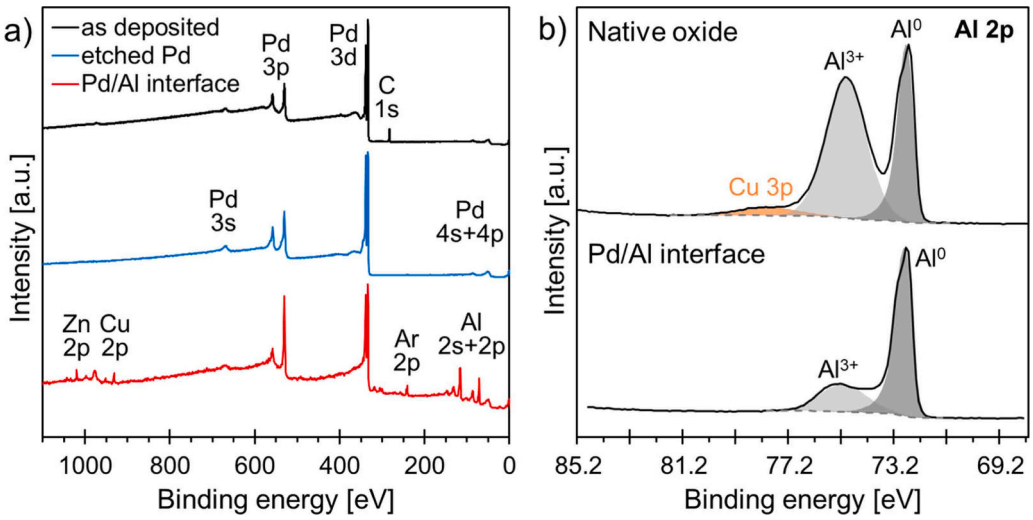

Fig. 3. XPS analysis of the interface of a sputter etched and coated Al alloy/Pd membrane for permeation tests a) survey spectra obtained for different steps during Ar^+ sputter depth profiling b) high resolution spectra of the Al 2p region obtained on a reference native oxide sample and a sputter etched and Pd coated sample of the same material.

sample of the same alloy with a native oxide layer formed after polishing is compared in Fig. 3b). Peak components of the metallic Al^0 spin-orbit and oxidized Al^{3+} are obvious at 72.5 eV and ~ 75.1 eV, respectively. In addition, a small Cu 3p signal can be seen for the native oxide sample. The Al^{3+}/Al^0 peak area ratios are ~ 1.8 for the native oxide case, while for the buried interface of the etched specimen it is significantly decreased to ~ 0.4.

3.2. Hydrogen permeation tests

For a further proof of concept of the effect of sputter etching during preparation, hydrogen permeation experiments on commercially pure Al foil with 30 μm thickness were performed on both sputter etched samples and samples that were directly Pd coated without removing the native oxide layer. The Pd side potential transients from hydrogen permeation tests on these samples are shown in Fig. 4. For both sample populations the Pd side OCP starts at a reproducible positive potential plateau close to the Nernst potential of the Pd/PdO transition [60], while it is slightly higher for the oxide interface samples (~290 mV_{SCE}) compared to the plasma etched samples (~260 mV_{SCE}). A rapid transition from this initial potential to a stable plateau is observed with both sample groups. Again, the final potential of the oxide interface samples (~-750 mV_{SCE}) is slightly higher and scatters more compared to the plasma etched samples (~-820 mV_{SCE}). The transition also occurs after a shorter time of 11.6 ± 0.1 h for the plasma etched samples compared to the oxide interface samples with 14 ± 1 h. It can be noted that the scatter between experiments is drastically reduced using sputter etched samples.

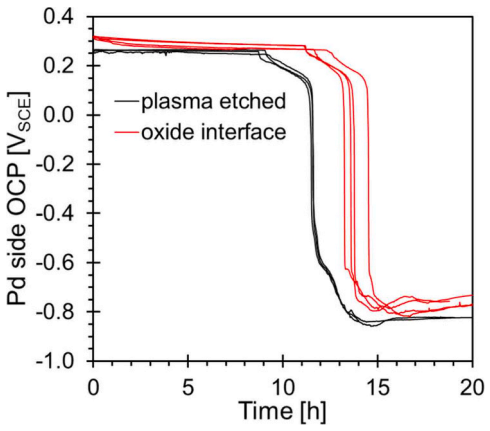

Fig. 4. Pd potential transients from hydrogen permeation tests on commercially pure Al foil samples (30 μm) with native oxide and sputter etched interfaces under the Pd coating.

In preparation of the hydrogen permeation tests on the commercial 7xxx alloys, the corrosion reaction on the H charging side was characterized for both alloys by immersion tests and cross section analysis of the corrosion front. The results of both analyses are shown in Fig. 5. The BSE images of the corroded samples in Fig. 5a) reveal a nearly uniform corrosion front for both materials after up to 1 week of immersion over wide areas of the sample surface. While the intermetallic particles in both alloys can interfere with the corrosion front (e.g. center of alloy B cross section) the deviations from this uniformity are relatively small due to the parallel orientation of the corroding surface and the rolling direction of the plate. Some corrosion product was observed above the corrosion front with drying cracks and clear detachment from the bulk material. Determination of the mass loss for varying immersion times further enabled the calculation of the time dependent corrosion rate of the alloys, as depicted in Fig. 5b). The corrosion reaction starts at very high rates for both alloys but quickly decays due to the buildup of corrosion products on the surface. A similar power-law like decay was observed in both cases, going from 0.7 to 1.0 μm/h after 6 h immersion towards a steady state of ~0.1 μm/h for longer immersion times > 90 h. Slightly higher corrosion rates are consistently observed for alloy A alongside a slightly higher R^2 value in the mathematical power-law function fit of the data.

Beside ex-situ immersion tests, the corrosion reaction in the hydrogen permeation tests was also monitored in-situ by measuring the OCP of the charging side of the membrane in the 0.01 M NaOH charging solution. In Fig. 6 three representative OCP curves for both alloys are displayed for comparison. A general trend of an initial sudden increase of the OCP followed by a slowed down drift of the potential towards more positive values is observed for both alloys. While the initial phase of rapid corrosion exhibits a similar potential rise, the two alloys' OCP values quickly diverge with the high Zn and low Cu alloy A showing potentials that are roughly 60–100 mV lower than that of the lower Zn and higher Cu containing alloy B. This potential difference lasted for the whole duration of the experiments. The stabilized potentials for longer running experiments did not exceed −1.36 V_{SCE} and −1.30 V_{SCE} for alloy A and B, respectively. Although minor deviations between experiments occurred for both alloys, the overall stabilization and drift

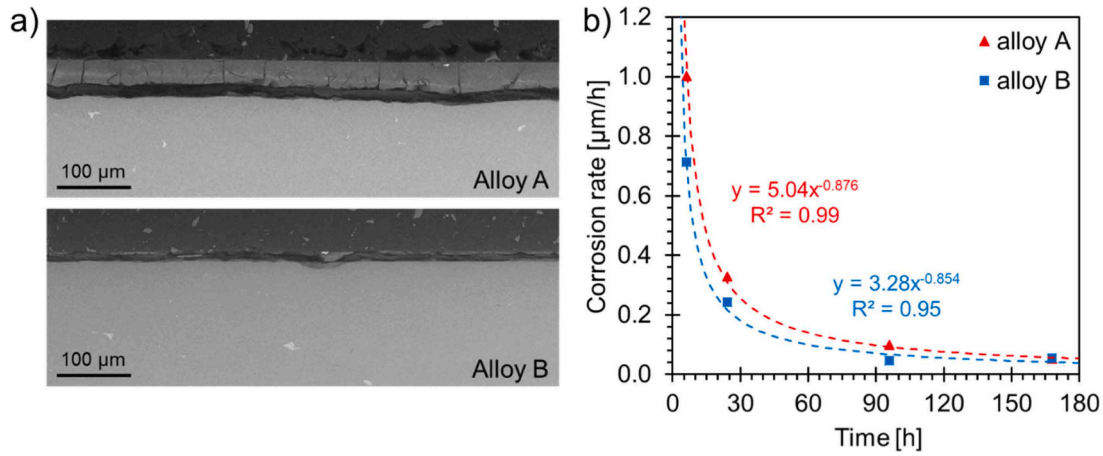

Fig. 5. Immersion tests for the characterization of the corrosion reaction for H charging. a) representative cross-section BSE images of samples left in 0.01 M NaOH solution for 1 week and b) time dependence of corrosion rates calculated from mass loss measurements with power-law function fit.

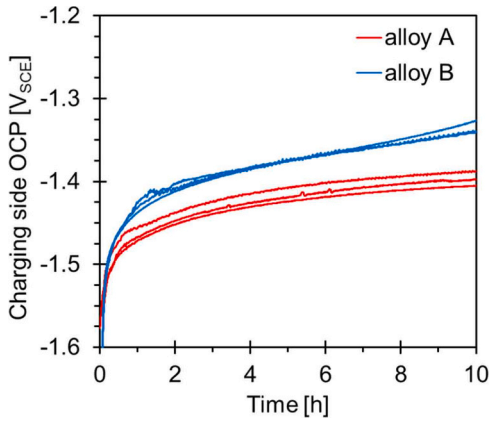

Fig. 6. Open circuit potential of the H charging side (Al alloy exposed to 0.01 M NaOH solution) during hydrogen permeation test.

behavior of the OCP was very similar and reproducible. Some experiments showed a minor periodic oscillation pattern of the OCP that was correlated to the formation and release of H_2 bubbles on the corroding surface. However, these oscillations did not affect the observations stated above.

The Pd side OCP transients obtained for the permeation experiments using both commercial alloys are displayed in Fig. 7. Numerous transients with varying membrane thicknesses were obtained for alloy A in Fig. 7a). The overall transient shapes are very comparable to those obtained on commercially pure Al foil in Fig. 4. However, some curves show more irregular fluctuations of the Pd potential, especially before the major H induced transition to −0.7 to −0.8 V_{SCE}. The delay at which the Pd OCP transient appears generally correlates well with the initial foil thickness. However, some samples break out of this ordering (e.g. 45 µm vs. 50 µm). Although very similar, the slopes of the transients are not perfectly identical, as obvious for the samples with 105 and 106 µm initial thickness. This example also demonstrates good reproducibility of the data with almost identical permeation times for similar initial foil thickness. While for alloy A, a lot of "successful" permeation transients were obtained, the distribution of permeation results for alloy B in Fig. 7b) is far less populated despite a similar number of tests performed on both materials. Experiments without transient did not show obvious H induced changes in the Pd layer OCP for experiment times of up to one week. Two representative curves with no transient (65 µm and 103 µm) are illustrated for comparison and marked with an "x" in the end. Despite the lack of a rapid H induced transient, these curves still exhibit a continuous OCP decrease of up to 250 mV over the course of 80 h. "Successful" experiments seem to occur preferentially for smaller foil thickness (< 70 µm). However, the experiments with the major OCP transients exhibit similar features as alloy A: Some irregular fluctuations in the initial time of H charging followed by a steep potential drop. Again, the times of the permeation transient increase for increasing

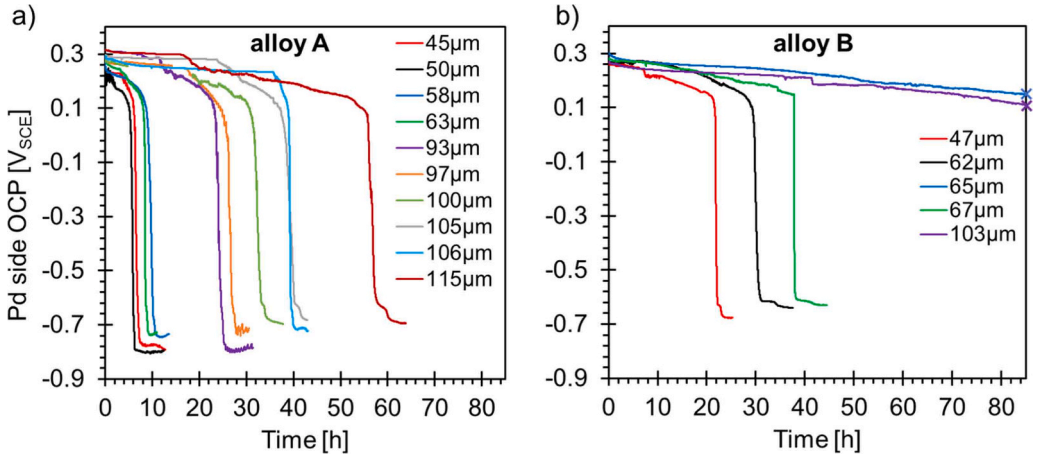

Fig. 7. OCP transients of the Pd coated H detection side in 0.1 M PBS, affected by the start of H generation during free corrosion on the charging side at t = 0, using various membrane thicknesses for a) alloy A and b) alloy B.

initial membrane thickness, which is consistent with the observation for alloy A. A comparison of membranes with a similar thickness in both alloys (e.g. "alloy A 63 μm" versus "alloy B 62 μm") revealed a much longer time lag before permeation in alloy B relative to alloy A. In addition, the plateau after the transient for alloy B at about −650 mV seems to be slightly higher in potential compared to alloy A.

By calculating the corrected foil thickness and determining the $t_{0.63}$ value for each transient, the effective hydrogen diffusion coefficient can be obtained following the time lag approach [35]. The resulting plot of the quadratic corrected thickness vs. the permeation time is given in Fig. 8. Linear fits are included for both alloys alongside the respective linear equations and coefficients of determination (R^2). R^2 for alloy A (0.94) is significantly higher compared to alloy B (0.82) with its limited experimental data, resulting in a larger uncertainty for the calculated diffusion coefficient. The effective hydrogen diffusion coefficients of alloy A and B can be determined as $D_{H,eff}$ (A) = 3.7 ± 0.3 × 10^{-10} cm^2/s and $D_{H,eff}$ (B) = 1.6 ± 0.7 × 10^{-10} cm^2/s, respectively.

3.3. Microstructural characterization of grain boundaries

The microstructure of the investigated alloys was characterized at the micro- and sub-micrometer scale to enhance the understanding of the observed H diffusion and trapping behavior in the hydrogen permeation tests. Representative backscatter electron images of the microstructure are provided in Fig. 9. The sample orientation was chosen to represent cross-sections of permeation membrane samples, where H diffusion would take place in ST direction from left to right. Alloy A in Fig. 9a) exhibits a very "clean" microstructure with grains slightly elongated in the L direction. Only a small number of polygonal Al_7Cu_2Fe particle clusters were observed, that are oriented along the rolling direction of the plate. The overall area fraction of these particle clusters amounts 0.17 ± 0.06 %. Alloy B, however, exhibits a much higher particle density of both polygonal Al_7Cu_2Fe particles and also round S phase (Al_2CuMg) particles, that sometimes nucleate on the former. Although not visible in the picture, round Mg_2Si particles were also occasionally observed in this alloy. The overall area fraction of Cu containing intermetallic particles in this alloy was 0.40 ± 0.11 %, which is roughly twice as high compared to alloy A.

High-angle grain boundaries (HA-GBs) as primary diffusion pathways for hydrogen were investigated by STEM and EDX. Fig. 10 shows representative micrographs of the HA-GBs in alloy A (a) and B (b) with corresponding EDX maps. In both cases the grain boundary region is covered by η-Mg(Zn,Cu,Al)$_2$ precipitates, which is backed up by the presence of Zn, Mg and Cu in the EDX maps. However, the precipitate morphology is quite different: Several continuously distributed precipitates in the range of ~20–200 nm cover the grain boundary in alloy A. These precipitates are elongated along the GB plane. In alloy B, the homogeneous coverage is frequently interrupted by larger quench-induced precipitates > 400 nm [62] of the same type, as seen in Fig. 10 b). These larger precipitates were observed to vary significantly in size with some ranging over 1000 nm e.g. on triple points. EDX point spectra of some grain boundary precipitates were also recorded on both alloys. No statistically significant variation of the chemistry of the small continuously distributed precipitates was observed. However, the large grain boundary precipitates in alloy B exhibited a lower Zn and higher Cu content than the smaller particles. A Cliff-Lorimer extrapolation plot [63] to distinguish the Al in the phase and the matrix background is given in Figure A 2 in the appendix, despite the low number of precipitates probed.

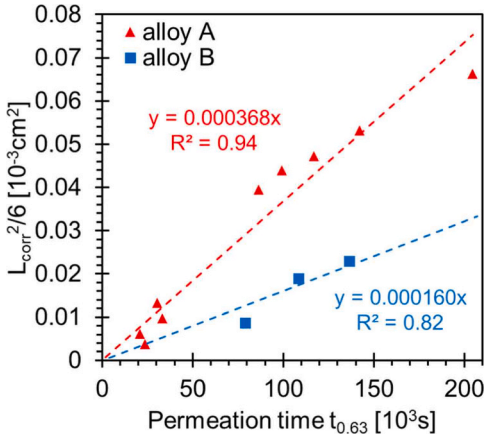

Fig. 8. Summary of diffusion data from hydrogen permeation experiments with corrosion corrected foil thicknesses. Linear fits were included to determine the effective H diffusion coefficients from the slope based on Fick's laws of diffusion.

4. Discussion

4.1. Advancements in sample preparation and methodology

The measurement of hydrogen diffusivity by permeation experiments for technical Al alloys come with a variety of additional challenges compared to e.g. steels, where this method is most commonly applied. The three main issues identified from the literature are:

1. The fcc structure and low H lattice solubility of solid Al leads to slow absorption and diffusion of H compared to bcc structured Fe.
2. The ubiquitous oxide layer can act as an additional diffusion barrier for H.
3. The complex microstructure of precipitation hardened Al alloys contains several constituent particles depending on the composition and processing, with each exhibiting a different potency for H trapping.

Within this study, these issues were systematically tackled by adapting and modifying a recently developed open circuit corrosion approach for Al alloys from the literature [53–55] and applying it to thick plate material of the microstructurally more complex Al-Zn-Mg-Cu alloy group.

To enable electrochemical H permeation tests on Al base materials, the driving force for H charging on the entrance side must be sufficiently high, while also ensuring a well-defined surface state without additional diffusion barriers, such as oxide layers. By choosing a corrosion environment at the open circuit potential for H charging from Hebert and Scully [53–55,64], we ensured a continuous source of absorbed hydrogen from an active corrosion front directly at the material surface. Given the violent nature of the corrosion reaction between Al and NaOH, it can be assumed that sufficient H fugacity is produced to establish a steady state diffusion profile through the alloy membranes [53,64]. This is also demonstrated by the successful transients obtained in the permeation experiments. However, this assumption comes with a time limitation that is obvious from the immersion tests in the charging solution in Fig. 5. While the uniform corrosion front is essential for the reliable determination of the membrane thickness at any time, the decay of the corrosion rate due corrosion product formation on the surface leads to a time limitation of these experiments up to approximately 80 h in this study. Moving beyond this point will lead to a drastic decrease of the H fugacity on the entry side that will in turn no longer be sufficient to establish a steady-state diffusion profile. Despite the assumption of a constant corrosion rate in the literature [54,55], we could not observe any transients past the 80 h mark and instead the Pd potential stabilized or even slightly recovered around 5–7 days into the experiment. However, the alloy composition and the nature and amount of corrosion product formed on the surface are pivotal for this limitation. Hence, the time dependence of the corrosion rate should always be re-assessed for hydrogen permeation tests on other alloy compositions. Even though

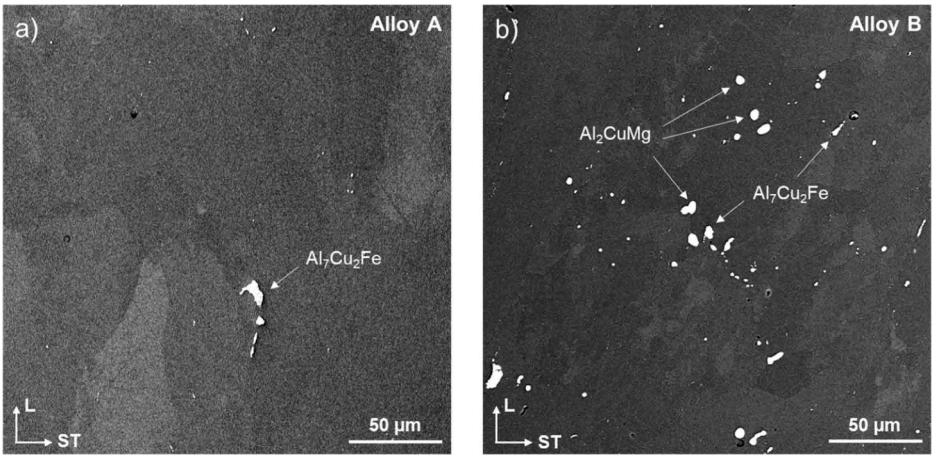

Fig. 9. Representative backscatter electron images of the microstructure of both alloys with different amounts of Cu containing intermetallic particles a) alloy A and b) alloy B.

dynamic conditions may introduce some uncertainty with this kind of hydrogen charging, it provides uniform and oxide free charging conditions with a high H fugacity at the active corrosion front and allows for direct comparisons between similar material systems with comparable corrosion rates. This unique combination of properties is not fulfilled with standard potentiostatic or galvanostatic charging methods.

Due to the decay of H fugacity at the charging side and the generally slow diffusion of H in Al base materials, sufficiently thin samples are paramount to achieve reasonable permeation times. Samples in the range of 20–120 µm were shown to be suitable for this kind of experiment [54,55]. During thinning of the samples great care should be taken not only because coating and handling these samples can be a delicate task, but also because this length scale can be relevant for microstructural features of technical Al alloys. Coarse constituent particles or particle clusters might occur in the membranes depending on the purity and processing of these alloys. Even though these particles are typically not fully avoidable, we present in this work how a careful selection of the sampling direction might benefit the measurement. By avoiding elongated particles in the thickness direction of the foil, we minimized the risk that these particles alter the uniformity of the corrosion front or even perforate the entirety of the alloy membrane. In addition, the anisotropy of the grain morphology should be considered for the evaluation of potential diffusion pathways in the respective alloy.

The native oxide layer formed on Al and its alloys is long known to be a very effective diffusion barrier for hydrogen [47,48]. While the oxide layer on the charging side is dissolved by the corrosive NaOH environment, the native oxide under the Pd coating on the detection side might influence the obtained results. Hence, we chose to adapt the sputter etching approach for native oxide layer removal first mentioned by Braun et al. [49,50]. We first propose a detailed routine for the sputter etching and Pd coating procedure in a vacuum chamber, with additional surface analysis and reproducibility studies to prove its effectiveness. The XPS depth profiling was performed so that both Pd and the alloy substrate signal were clearly visible in the spectrum. This ensured that the measured interface is still buried under Pd and not damaged by the sputtering process, nor exposed to residual gas in the vacuum chamber of the instrument. The significant reduction of the Al^{3+}/Al^0 peak ratio compared to the native oxide surface is a direct evidence for the effectiveness of the sputter etching treatment. A slight over-estimation of the oxide signal would actually be expected because of the higher-up position of the oxide within the sample. This is backed up by the absence of the bulk Cu 3p signal in the high-resolution spectrum of the Pd coated sample vs the native oxide sample (Fig. 3b)), which is likely due to signal attenuation from the remaining Pd on the surface. Despite the described tendency for over-estimation of the oxide component at the buried interface, the residual signal from oxidized Al^{3+} is fairly low and likely coming from oxide islands, that formed when the bare metal surface reacted with residual O in the vacuum chamber used for coating. This re-oxidation can only take place in the < 5 s time of switching from sputter etching to Pd coating. We assume O from the residual gas in the chamber is not sufficient for the formation of a continuous oxide film within such a short duration, because of the low base pressure in the vacuum chamber and the continuous Ar flushing during the whole etching and coating procedure. Additional permeation experiments on Al foil with a very homogeneous microstructure were performed as a benchmark to isolate the effect of sputter etching on the actual permeation transients. As demonstrated in Fig. 4, we could not only speed up the permeation transients and therefore reduce the influence of the oxide, but also greatly enhance the reproducibility of the permeation experiments. This observation strengthens the suggested discontinuity of the residual oxide layer: A continuous residual oxide layer after etching would expectedly result in faster permeation times but also replicate the initial scatter to some extent. The complete removal of the oxide layer, however, would lead to the fastest possible permeation time, that is purely bulk microstructure controlled. I.e., by design, the scatter should be very small for the homogeneous Al foil samples. We assume the latter case is observed, since the scatter after sputter etching is practically eliminated. It is likely, that small residual oxide islands could be easily bypassed by short-distance H diffusion along the interface and therefor result in a factual elimination of the oxide layer as a source of error. In addition, the large delays caused by the nm thin oxide film in Fig. 3 suggest that there might be an enhanced transition of H from the bulk alloy to the Pd film due to enhanced interfacial bonding and potential lattice mismatch stresses. Thus, the described practice for minimizing the native oxide film allowed us to investigate hydrogen permeation that is purely affected by the bulk material and its microstructural features.

The microstructure of the investigated Al alloys is often very complex depending on the alloy compositions. Constituent phases and their interfaces are known to exhibit varying degrees of H trapping capabilities, which can lead to a significant delay of the permeation signal [29,30,51,52,65]. In combination with the generally low H solubility within Al, this often causes long experiment times and low amounts of detectable H on the exit side of the membranes. The adapted approach from Hebert and Scully [53–55] allows for the detection of small amounts of H by using the unique H sensing capabilities of thin films of Pd. Even small amounts of H permeation will quickly saturate the film and cause the formation of PdH_x, which will in turn lead to a measurable drop of the electrochemical potential [53,56]. In combination with the utilization of thin samples in the < 120 µm range, we were able to detect permeation

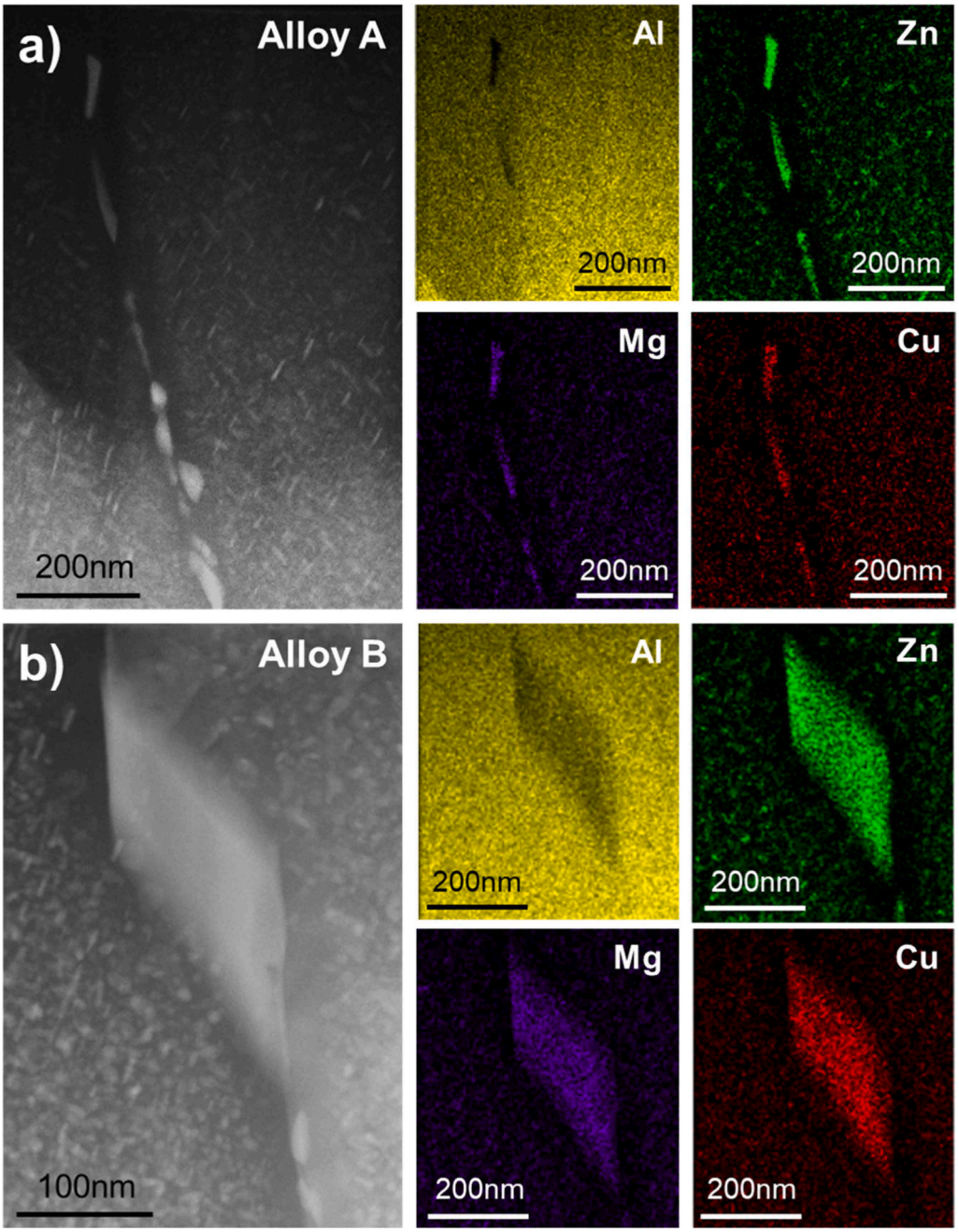

Fig. 10. STEM micrographs of HA-GB covered with precipitates and EDX mapping of Al, Zn, Mg, Cu in a) alloy A and b) alloy B.

transients even for overaged Al-Zn-Mg-Cu alloys that are known to be full of various H trap sites [51]. Due to the area integral nature of hydrogen permeation tests, no direct conclusions about the exact pathways of H within the material can be made. However, similar materials (i.e. similar compositions and processing) may be compared to gain knowledge about the hydrogen mobility and the amounts of irreversible H traps within the alloy materials, as recently demonstrated by Akuata et al. [59]. Hence, the presented method is an approachable way to elucidate the potential role of H mobility in e.g. stress-corrosion cracking.

4.2. Hydrogen diffusion and trapping in commercial 7xxx series alloys

This study presents the first set of hydrogen permeation tests comparing third (A) and second generation (B) 7xxx series Al alloys using the above-mentioned improved methodology. We report the $D_{H,eff}$ for the high Zn, high purity third generation alloy A exceeds $D_{H,eff}$ of the second generation alloy B by roughly a factor of two. As demonstrated above, these changes of the observed H diffusivity can be allocated almost entirely to the microstructure of the membrane samples.

The corrosion reaction on the charging side is only minorly affected by microstructure and chemistry of the alloys. While the corrosion potential in the 0.01 M NaOH charging solution in Fig. 6 deviate slightly in accordance with the different alloy chemistry [66], the observed corrosion rates from the immersion tests (Fig. 5) show very similar behavior. Especially in the beginning of the immersion experiment, the corrosion rate, i.e. also the hydrogen fugacity, is very high. Minor differences in the enrichment of alloying elements below the native oxide [67] are assumed to have minimal effect under these conditions. Hence, we assume similar boundary conditions for H diffusion with both alloys. Coarse intermetallic particles might have a larger influence on the corrosion front, as they can both create lateral inhomogeneity and also

contain larger amounts of alloying elements that will enhance the formation of corrosion products on the surface [68,69]. Hence, the slightly lower quality fit and the overall slightly lower corrosion rate in alloy B is likely caused by the higher amount of intermetallic particles in alloy B. Especially the finely distributed S phase particles cannot be fully avoided during sampling. Overall however, the corrosion system on the charging side can be well described with the proposed power-law approach.

Comparing the benchmark experiments on pure Al with the potential transients of the alloy material, some differences can be immediately identified:

1. The initial onset of the Pd potential transient of the Al foil exhibits a clear kink in the signal compared to a more continuous decay for the commercial alloys.
2. The large potential drop for the Al foil samples is almost instantaneous while the slopes vary significantly for the alloy membranes.
3. The final plateau potential after the PdH_x transition scatters much more for the commercial alloys with slightly higher final potentials for longer permeation times.

1. and 2. can be explained by the area integral nature of the permeation experiment. During the onset of the permeation transient we suggest a spot like permeation along some grain boundaries, which will result in a mixed potential with some areas of H filled Pd and some Pd at the initial potential. Surface polarization by hydride islands, lateral diffusion of H along the Al/Pd interface, and diffusion within the Pd coating might then cause a continuous decay of the potential and depending on the number of permeation sites and the H flux, the PdH_x transition might happen at different rates, i.e. slopes of the transient. Since Al foil typically exhibits a very fine grain structure [70] and almost no constituent particles, we observe an almost step-like permeation transient with a mostly homogeneous H diffusion front and many permeation sites. In the case of the thick plate 7xxx series alloys, the pancake shaped grains are larger [25] and the grain boundaries are covered with particles, that can potentially trap and limit the diffusion of H. Thus, the potential decay can appear in a wide range of shapes and some noise-like fluctuations of the potential were observed. Finally, 3. is assumed to be related to the H flux on the exit side of the membrane. If the transient occurs after short time, there is a higher likelihood for an abundance of H on the exit side, leading to an even lower PdH_x potential [56,57] compared to longer permeation times with significantly reduced H fugacity on the entry side of the foil and potentially stronger H trapping.

The major reason for the observed different permeation results between the two alloys lies in the different H trapping behavior of the microstructure. Hence, additional microstructural analysis of both coarse intermetallic particles and the grain boundary precipitates was performed to understand this effect on H diffusion. As expected from the literature, the lower purity alloy B contains a higher density of Cu containing intermetallic particles like Al_7Cu_2Fe and S-phase alongside some Mg_2Si, while the higher purity alloy A only exhibits some Al_7Cu_2Fe [25]. Fig. 11 summarizes the literature on DFT calculated H trap energies of these intermetallic particles with respect to some other common microstructural features [16,17,65,71]. Al_7Cu_2Fe has the highest H trapping energy of all listed features, while S-phase can also trap H about as well as a (pure Al) grain boundary. Mg_2Si however, exhibits no stable H trap sites. The trapping capabilities of Al_7Cu_2Fe and S-phase were also experimentally confirmed with H concentrations in these large phases ranging up to 10 and 5 at%, respectively [11,31]. Hence, we assume the higher amount of Cu containing intermetallic particles can likely act as a H sink in the permeation experiment. The permeation transient will be delayed until these sinks are saturated with H and the steady-state diffusion profile can only be established if there is still enough H fugacity available after that. Considering the size and the high H concentrations needed for saturation of these particles, we assume this is the main reason for the lower $D_{H,eff}$ observed for alloy B.

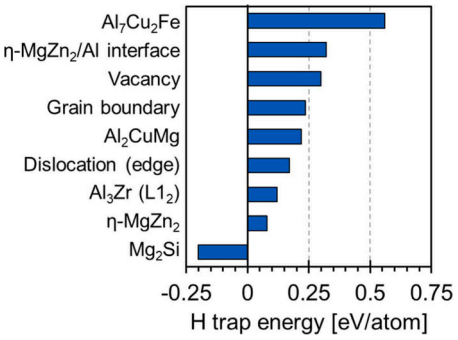

Fig. 11. Trapping energies for relevant constituent phases and microstructural features in the investigated Al-Zn-Mg-Cu alloys calculated by DFT [16,65,71].

Most of the remaining features from Fig. 11 cannot be correlated to the permeation results, since no major differences are expected with the same temper and plate thickness of the alloys. The grain boundary η-phase however, was recently shown to exhibit different morphology and chemical compositions depending on the alloy composition and the corresponding quench-sensitivity [62]. In agreement with this study, the quench-induced grain boundary precipitates in a more quench-sensitive alloy were shown to be very large (up to 2 μm) with an almost two-dimensional snowflake-like morphology covering the grain boundaries. Their chemistry also exhibits higher Cu and lower Zn levels compared to the aging-induced precipitates [62,72]. This distinction was particularly obvious in alloy B, where similar trends could be observed despite the lower number of precipitates probed by EDX. While the interior of these particles does not act as a deep hydrogen trap, their interfaces can be very effective depending on the termination of the phase [16]. Even though the interfacial H trap energy of an actual η-phase, containing Cu and Al, is not known, a potential Mg termination of these lower Zn precipitates might give rise to a substantial trapping capability. Thus, we suggest that the large interface area of the quench-induced η-phase on the grain boundaries additionally hampers H diffusion in alloy B. A schematic summarizing the proposed diffusion and trapping mechanisms along the grain boundaries in the investigated overaged Al-Zn-Mg-Cu alloys is given in Fig. 12. A rigorous quantitative assessment of the trap sites in these alloys would require precise knowledge of the initial trap occupancy induced by the material processing and sample preparation prior to the experiment. However, the differences of the initial bulk H content in commercially produced material are considered insignificant considering the large amount of available irreversible trap sites, especially in the Cu containing intermetallic particles mentioned above. The long permeation times required to achieve trap saturation under the high fugacity H charging conditions suggest no significant trap occupancy prior to the permeation experiment, rendering permeation measurements a robust tool to study the microstructural influence on H diffusion in commercial Al alloys.

As mentioned above, comparisons between the obtained $D_{H,eff}$ values and literature data cannot easily be made because of the crucial role of microstructural trap sites and, in this case, the lack of other studies. However, the presented data can be put into perspective with thermal desorption data on an overaged 7050 alloy [28], that is close to the composition of alloy B. The room temperature diffusion coefficient of 3.15×10^{-9} cm^2/s lies within a reasonable order of magnitude compared to the $1.6 \pm 0.7 \times 10^{-10}$ cm^2/s presented in this work, considering the different methodology and different processing of the alloys. A much better comparison can be made with the recent results from Akuata et al. [59] that were obtained using the same method in the same lab as this study. Despite a significantly higher level of Fe and Si and primary phase fraction, similar $D_{H,eff}$ values were obtained for a lab cast 7449 alloy (2.2×10^{-10} cm^2/s and alloy A in this work ($3.7 \pm 0.3 \times 10^{-10}$ cm^2/s). This underlines the importance of alloy

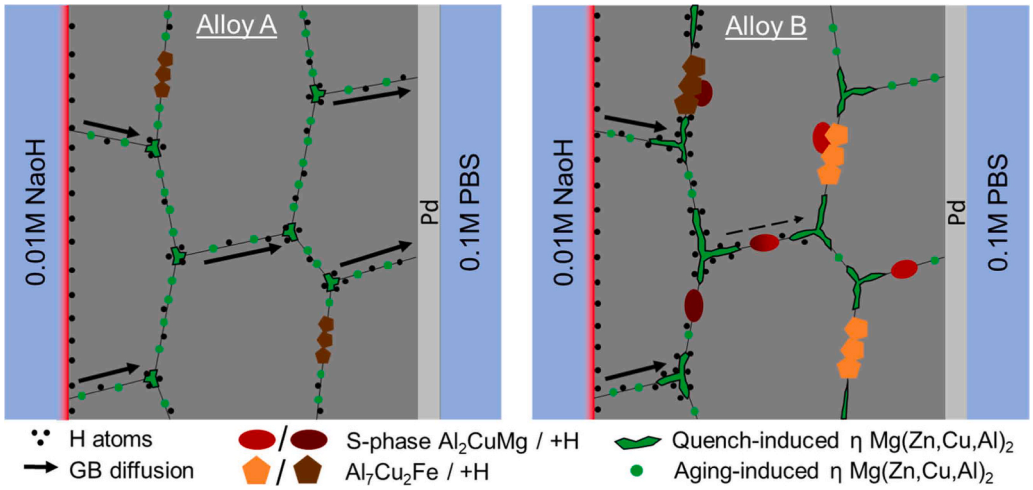

Fig. 12. Schematic depiction of proposed diffusion and trapping mechanisms in the investigated Al-Zn-Mg-Cu alloys leading to different H permeation test results.

processing: Even though much slower diffusion would be expected with the higher primary phase fraction of the lab cast alloy, the small-scale processing caused a significantly smaller grain size compared to commercial thick plate material [25]. This larger number of diffusion pathways in the diffusion direction can justify the observed similar hydrogen diffusivity. Correlating the obtained hydrogen diffusivities in the bulk alloys with HEAC susceptibility, it should be noted that the applied stress in mechanical testing might significantly enhance the effective hydrogen diffusivity by dislocation transport [73–75]. Hence, the relatively low $D_{H,eff}$ values do not rule out a H transport control, even if the crack tip moves longer distances than what could be theoretically covered by bulk diffusion. Both this study and that of Akuata et al. reveal a positive correlation between $D_{H,eff}$ and HEAC susceptibility of some high Zn 7xxx series alloys [25,59]. This implies H transport is a rate limiting step for HEAC in these alloys and simultaneously reveals a high potential for hydrogen permeation testing to characterize and analyze H induced cracking.

5. Conclusions

In this study we present an improved electrochemical H permeation testing method for the reliable characterization H diffusion and trapping in Al and its alloys, involving a best practice routine for sputter etching and coating of membrane samples in combination with the alkaline corrosion H charging approach by Hebert et al. [53–55]. The first H permeation dataset comparing third and second generation 7xxx series Al alloys was obtained with this method and the following conclusions were drawn:

- Sputter etching of the native oxide film is an effective measure to improve the quality of electrochemical hydrogen permeation data. We demonstrate unprecedented experimental reproducibility on pure Al samples alongside a detailed guideline for sample preparation.
- The effective hydrogen diffusivity of the third-generation alloy A with higher purity and Zn content was twice as large as for the 2nd-generation alloy B.
- Coarse intermetallic Al_7Cu_2Fe and Al_2CuMg (S-phase) particles with a high trapping energy in alloy B can bind large amounts of H, effectively delaying hydrogen permeation.
- Quench-induced grain boundary η-$Mg(Zn,Al,Cu)_2$ particles with lower Zn content in alloy B may be able to trap H at their interfaces much more effectively compared to aging-induced precipitates.

CRediT authorship contribution statement

Daniela Zander: Writing – review & editing, Supervision, Funding acquisition. **Oliver Beyss:** Writing – review & editing, Writing – original draft, Methodology, Investigation, Formal analysis, Data curation, Conceptualization. **Chijioke Kenneth Akuata:** Writing – review & editing, Methodology. **Laura Kopruch:** Writing – review & editing, Methodology.

Declaration of Competing Interest

The authors declare that they have no known competing financial interests or personal relationships that could have appeared to influence the work reported in this paper.

Acknowledgement

The authors gratefully acknowledge the Airbus Advanced Metal Research Program (AMRP) for the funding. We personally thank Christian Engel (Airbus Operations GmbH), Dr. Matthias Knüwer (Airbus Operations GmbH) and Theo Hack (Airbus S.A.S.) for frequent exchange on the topic. Moreover, we thank Martina Thönnissen, Lucia Pilotta, Luka Brommont, and Braveen Paskaran for their support with sample preparation, immersion and permeation tests.

Appendix

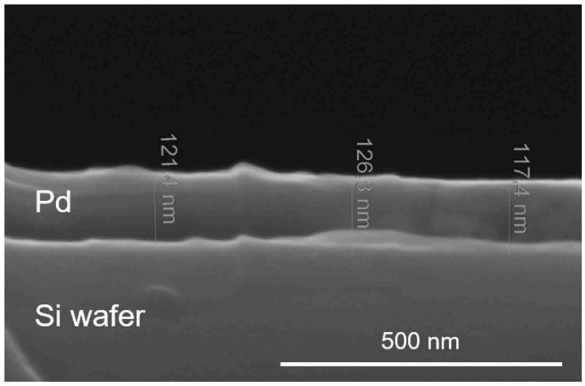

Figure A 1. SEM cross-section of a Pd coated Si wafer dummy. Test coating was performed for 7 min resulting in a coating thickness of around 120 nm. The duration of the coating was then adjusted to 3 min to achieve approximately 50 nm Pd coating on the alloy samples used in the permeation experiments

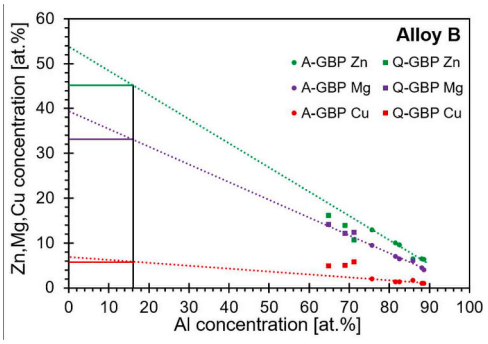

Figure A 2. Cliff Lorimer extrapolation plot for aging-induced grain boundary precipitates (A-GBPs) in alloy B. Quench-induced grain boundary precipitate (Q-GBP) compositions are given for reference, where Cu is increased and Zn reduced compared to the A-GBPs

Data availability

The data that has been used is confidential.

References

[1] Y. Sun, The use of aluminum alloys in structures: review and outlook, Structures 57 (2023) 105290.
[2] E.A. Starke, J.T. Staley, Application of modern aluminum alloys to aircraft, Prog. Aerosp. Sci. 32 (1996) 131–172.
[3] N.J.H. Holroyd, T.L. Burnett, J.J. Lewandowski, G.M. Scamans, Environment-induced cracking of high-strength Al-Zn-Mg-Cu aluminum alloys: past, present, and future, Corrosion 79 (2022) 48–71.
[4] J.C. Williams, E.A. Starke, in: S. Suresh (Ed.), Progress in structural materials for aerospace systems11The Golden Jubilee Issue—Selected topics in Materials Science and Engineering: Past, Present and Future, Acta Materialia, 2003, pp. 5775–5799.
[5] R.T. Euesden, M.E. Curd, Y. Yao, C. Grant, N.J.H. Holroyd, P.B. Prangnell, T. L. Burnett, Direct comparison of the environmentally induced cracking resistance of 2nd and 3rd generation alloys, AA7050-T7651 and AA7085-T7651, Mater. Des. 253 (2025) 113867.
[6] W.S. Miller, L. Zhuang, J. Bottema, A.J. Wittebrood, P.De Smet, A. Haszler, A. Vieregge, Recent development in aluminium alloys for the automotive industry, Materials Science Engineering A 280 (2000) 37–49.
[7] T. Trzepieciński, S.M. Najm, Current Trends in Metallic Materials for Body Panels and Structural Members Used in the Automotive Industry, Materials 17 (2024) 590.
[8] B. Zhou, B. Liu, S. Zhang, The advancement of 7XXX series aluminum alloys for aircraft structures: a review, Metals 11 (2021) 718.
[9] L. Rickard, A. Bampoulas, M. Laad, E. Mangina, AI-driven optimisation of metal alloys for space applications, Discov. Artif. Intell. 5 (2025) 35.
[10] M. Barucci, L. Risegari, E. Olivieri, E. Pasca, G. Ventura, ALUMINIUM ALLOYS FOR SPACE APPLICATIONS: LOW TEMPERATURE THERMAL CONDUCTIVITY OF A6061-T6 AND A1050, in: Astroparticle, Particle and Space Physics, Detectors and Medical Physics Applications, pp. 541-545.
[11] H. Zhao, P. Chakraborty, D. Ponge, T. Hickel, B. Sun, C.-H. Wu, B. Gault, D. Raabe, Hydrogen trapping and embrittlement in high-strength Al alloys, Nature 602 (2022) 437–441.
[12] S. Evers, M. Rohwerder, The hydrogen electrode in the “dry”: a Kelvin probe approach to measuring hydrogen in metals, Electrochem. Commun. 24 (2012) 85–88.
[13] B. Gault, A. Saksena, X. Sauvage, P. Bagot, L.S. Aota, J. Arlt, L.T. Belkacemi, T. Boll, Y.-S. Chen, L. Daly, M.B. Djukic, J.O. Douglas, M.J. Duarte, P.J. Felfer, R.G. Forbes, J. Fu, H.M. Gardner, R. Gemma, S.S.A. Gerstl, Y. Gong, G. Hachet, S. Jakob, B. M. Jenkins, M.E. Jones, H. Khanchandani, P. Kontis, M. Krämer, M. Kühbach, R.K. W. Marceau, D. Mayweg, K.L. Moore, V. Nallathambi, B.C. Ott, J.D. Poplawsky, T. Prosa, A. Pundt, M. Saha, T.M. Schwarz, Y. Shang, X. Shen, M. Vrellou, Y. Yu, Y. Zhao, H. Zhao, B. Zou, Towards establishing best practice in the analysis of hydrogen and deuterium by atom probe tomography, Microsc. Microanal. 30 (2024) 1205–1220.
[14] H. Kakinuma, S. Ajito, T. Hojo, M. Koyama, E. Akiyama, Real-time visualization of hydrogen distribution in metals using polyaniline: an ultrasensitive hydrogenochromic sensor, Adv. Mater. Interfaces 9 (2022) 2101984.
[15] D.S. Sholl, Using density functional theory to study hydrogen diffusion in metals: a brief overview, J. Alloy. Compd. 446-447 (2007) 462–468.
[16] T. Tsuru, M. Yamaguchi, K. Ebihara, M. Itakura, Y. Shiihara, K. Matsuda, H. Toda, First-principles study of hydrogen segregation at the MgZn2 precipitate in Al-Mg-Zn alloys, Comput. Mater. Sci. 148 (2018) 301–306.
[17] T. Tsuru, K. Shimizu, M. Yamaguchi, M. Itakura, K. Ebihara, A. Bendo, K. Matsuda, H. Toda, Hydrogen-accelerated spontaneous microcracking in high-strength aluminium alloys, Sci. Rep. 10 (2020) 1998.
[18] X. Zhou, F.El Gabaly, V. Stavila, M. Allendorf, Molecular dynamics simulations of hydrogen diffusion in aluminum, J. Phys. Chem. C. 120 (2016) 7500–7509.
[19] Y. Chen, S. Zhao, H. Ma, H. Wang, L. Hua, S. Fu, Analysis of hydrogen embrittlement on aluminum alloys for vehicle-mounted hydrogen storage tanks: a review, Metals 11 (2021) 1303.
[20] Q. Cheng, R. Zhang, Z. Shi, J. Lin, Review of common hydrogen storage tanks and current manufacturing methods for aluminium alloy tank liners, Int. J. Lightweight Mater. Manuf. 7 (2024) 269–284.
[21] M.O. Speidel, Stress corrosion cracking of aluminum alloys, Metall. Trans. A 6 (1975) 631–651.
[22] N.J.H. Holroyd, G.M. Scamans, Crack propagation during sustained-load cracking of Al-Zn-Mg-Cu aluminum alloys exposed to moist air or distilled water, Metall. Mater. Trans. A 42 (2011) 3979–3998.
[23] N.J.H. Holroyd, G.M. Scamans, Stress corrosion cracking in Al-Zn-Mg-Cu aluminum alloys in saline environments, Metall. Mater. Trans. A 44 (2013) 1230–1253.

[24] S. Knight, K. Pohl, N. Holroyd, N. Birbilis, P. Rometsch, B. Muddle, R. Goswami, S. Lynch, Some effects of alloy composition on stress corrosion cracking in Al–Zn–Mg–Cu alloys, Corros. Sci. 98 (2015) 50–62.
[25] E. Schwarzenböck, E. Ollivier, A. Garner, A. Cassell, T. Hack, Z. Barrett, C. Engel, T. L. Burnett, N.J.H. Holroyd, J.D. Robson, P.B. Prangnell, Environmental cracking performance of new generation thick plate 7000-T7x series alloys in humid air, Corros. Sci. 171 (2020) 108701.
[26] N.J.H. Holroyd, T.L. Burnett, J.J. Lewandowski, G.M. Scamans, Crack initiation during environment-induced cracking of metals: current status, Corros. Rev. 42 (2024) 523–542.
[27] G. Young, Jr, J. Scully, The diffusion and trapping of hydrogen in high purity aluminum, Acta Mater. 46 (1998) 6337–6349.
[28] J. Scully, G. Young, Jr, S. Smith, Hydrogen solubility, diffusion and trapping in high purity aluminum and selected Al-base alloys. Materials Science Forum, Trans Tech Publ, 2000, pp. 1583–1600.
[29] M.S. Bhuiyan, H. Toda, Z. Peng, S. Hang, K. Horikawa, K. Uesugi, A. Takeuchi, N. Sakaguchi, Y. Watanabe, Combined microtomography, thermal desorption spectroscopy, X-ray diffraction study of hydrogen trapping behavior in 7XXX aluminum alloys, Materials Science Engineering A 655 (2016) 221–228.
[30] M.S. Bhuiyan, H. Toda, Z. Peng, S. Hang, K. Horikawa, K. Uesugi, A. Takeuchi, N. Sakaguchi, Y. Watanabe, Corrigendum to "Combined microtomography, thermal desorption spectroscopy, X-ray diffraction study of hydrogen trapping behavior in 7XXX aluminum alloys" [Mater. Sci. Eng. A 655 (2016) 221–228], Materials Science Engineering A 668 (2016) 271–272.
[31] H. Kamoutsi, G.N. Haidemenopoulos, V. Bontozoglou, P.V. Petroyiannis, S. G. Pantelakis, Effect of prior deformation and heat treatment on the corrosion-induced hydrogen trapping in aluminium alloy 2024, Corros. Sci. 80 (2014) 139–142.
[32] H. Kamoutsi, G.N. Haidemenopoulos, H. Mavros, C. Karantonidis, P. Floratos, Z. Alhosani, P. Cho, D.H. Anjum, F. Ravaux, K. Polychronopoulou, Effect of precipitate coherency on the corrosion-induced hydrogen trapping in 2024 aluminum alloy, Int. J. Hydrog. Energy 46 (2021) 34487–34497.
[33] S. Xiukui, X. Jian, L. Yiyi, Hydrogen permeation behaviour in austenitic stainless steels, Materials Science Engineering A 114 (1989) 179–187.
[34] W. Song, J. Du, Y. Xu, B. Long, A study of hydrogen permeation in aluminum alloy treated by various oxidation processes, J. Nucl. Mater. 246 (1997) 139–143.
[35] M. Devanathan, Z. Stachurski, The adsorption and diffusion of electrolytic hydrogen in palladium, Proc. R. Soc. Lond. Ser. A. Math. Phys. Sci. 270 (1962) 90–102.
[36] A. Turnbull, Factors affecting the reliability of hydrogen permeation measurement. Materials Science Forum, Trans Tech Publ, 1995, pp. 63–78.
[37] R.J. Gest, A.R. Troiano, Stress corrosion and hydrogen embrittlement in an aluminum alloy, Corrosion 30 (1974) 274–279.
[38] P. Zhou, W. Li, H. Zhao, X. Jin, Role of microstructure on electrochemical hydrogen permeation properties in advanced high strength steels, Int. J. Hydrog. Energy 43 (2018) 10905–10914.
[39] R.H. Song, S. Pyun, Hydrogen permeation through a bilayer of Fe/electrodeposited Ni, J. Electrochem. Soc. 137 (1990) 1051.
[40] M. Paramasivam, S.V. Iyer, Influence of alloying additives on corrosion and hydrogen permeation through commercial aluminium in alkaline solution, J. Appl. Electrochem. 31 (2001) 115–119.
[41] A. Onuchukwu, S. Trasatti, Hydrogen permeation into aluminum alloy 1060 as a result of corrosion in alkaline medium. Basic features of the process, Electrochim. Acta 33 (1988) 1425–1430.
[42] O. Beyss, D. Zander, Characerization of the effective hydrogen diffusion in overaged 7xxx series Al alloys with a modified Devanathan-Stachurski permeation method, ICAA17, Grenoble, France, 2020.
[43] S. Ajito, H. Kakinuma, M. Koyama, E. Akiyama, Visualization of microscopic hydrogen diffusion in polycrystalline pure Ni using an Ir complex, Mater. Trans. 65 (2024) 1436–1441.
[44] M. Kupka, K. Stępień, K. Nowak, Studies on hydrogen diffusivity in iron aluminides using the Devanathan–Stachurski method, J. Phys. Chem. Solids 75 (2014) 344–350.
[45] A.Sf Testing, Materials, ASTM G148-97: Standard Practice for Evaluation of Hydrogen Uptake, Permeation, and Transport in Metals by an Electrochemical Technique, ASTM, 2018.
[46] M.J. Danielson, Use of the Devanathan–Stachurski cell to measure hydrogen permeation in aluminum alloys, Corros. Sci. 44 (2002) 829–840.
[47] N.-E. Laadel, M. El Mansori, N. Kang, S. Marlin, Y. Boussant-Roux, Permeation barriers for hydrogen embrittlement prevention in metals–a review on mechanisms, materials suitability and efficiency, Int. J. Hydrog. Energy 47 (2022) 32707–32731.
[48] Y. Yamada-Takamura, F. Koch, H. Maier, H. Bolt, Hydrogen permeation barrier performance characterization of vapor deposited amorphous aluminum oxide films using coloration of tungsten oxide, Surf. Coat. Technol. 153 (2002) 114–118.
[49] R. Braun, H. Schluter, H. Zuchner, H. Buhl, Hydrogen transport and cracking in metals, Inst. of Mater., Teddington, (1994).
[50] H.-J. Schlüter, H. Züchner, R. Braun, H. Buhl, Diffusion of hydrogen in aluminium, Z. Fuer Phys. Chem. 181 (1993) 103–109.
[51] L. Oger, M.C. Lafouresse, G. Odemer, L. Peguet, C. Blanc, Hydrogen diffusion and trapping in a low copper 7xxx aluminium alloy investigated by Scanning Kelvin Probe Force Microscopy, Mater. Sci. Eng. A 706 (2017) 126–135.
[52] L. Oger, B. Malard, G. Odemer, L. Peguet, C. Blanc, Influence of dislocations on hydrogen diffusion and trapping in an Al-Zn-Mg aluminium alloy, Mater. Des. 180 (2019) 107901.
[53] S. Adhikari, J. Ai, K.R. Hebert, K. Ho, C. Wang, Hydrogen in aluminum during alkaline corrosion, Electrochim. Acta 55 (2010) 5326–5331.
[54] J.-H. Ai, M.L.C. Lim, J.R. Scully, Effective hydrogen diffusion in aluminum alloy 5083-H131 as a function of orientation and degree of sensitization, Corrosion 69 (2013) 1225–1239.
[55] J.-H. Ai, J.R. Scully, Hydrogen diffusivity during corrosion of high-purity aluminum, Corrosion 69 (2013) 752–767.
[56] A.T. Landers, H. Peng, D.M. Koshy, S.H. Lee, J.T. Feaster, J.C. Lin, J.W. Beeman, D. Higgins, J. Yano, W.S. Drisdell, Dynamics and hysteresis of hydrogen intercalation and deintercalation in palladium electrodes: a multimodal in situ X-ray diffraction, coulometry, and computational study, Chem. Mater. 33 (2021) 5872–5884.
[57] A.M. Abdellah, F. Ismail, O.W. Siig, J. Yang, C.M. Andrei, L.-A. DiCecco, A. Rakhsha, K.E. Salem, K. Grandfield, N. Bassim, R. Black, G. Kastlunger, L. Soleymani, D. Higgins, Impact of palladium/palladium hydride conversion on electrochemical CO2 reduction via in-situ transmission electron microscopy and diffraction, Nat. Commun. 15 (2024) 938.
[58] M. Shao, X. Xing, C.C. Liu, pH measurements based on a palladium electrode, Electroanalysis 6 (1994) 245–249.
[59] C.K. Akuata, O. Beyß, L.T. Belkacemi, K. Hantzsche, M.E. Curd, D. Zander, On the impact of Cr and Ag additions on the grain boundary microchemistry, hydrogen permeability and environmentally assisted cracking mechanism of an Al-Zn-Mg-Cu-Zr 7xxx alloy, Corros. Sci. 246 (2025) 112759.
[60] M. Pourbaix, Atlas of Electrochemical Equilibria in Aqueous Solutions, NACE, Houston, 1974.
[61] A.Sf Testing, Materials, ASTM G1-03: Standard Practice for Preparing, Cleaning, and Evaluating Corrosion Test Specimens, ASTM, 2004.
[62] A. Garner, R. Euesden, Y. Yao, Y. Aboura, H. Zhao, J. Donoghue, M. Curioni, B. Gault, P. Shanthraj, Z. Barrett, C. Engel, T.L. Burnett, P.B. Prangnell, Multiscale analysis of grain boundary microstructure in high strength 7xxx Al alloys, Acta Mater. 202 (2021) 190–210.
[63] G. Cliff, D. Powell, R. Pilkington, P. Champness, G. Lorimer, 1983, Lorimer, X-ray microanalysis of second phase particles in thin foils, in: Conference series-Institute of physics, 1983, pp. 63-66..
[64] K.R. Hebert, Trapping of hydrogen absorbed in aluminum during corrosion, Electrochim. Acta 168 (2015) 199–205.
[65] Y. Xu, H. Toda, K. Shimizu, Y. Wang, B. Gault, W. Li, K. Hirayama, H. Fujihara, X. Jin, A. Takeuchi, M. Uesugi, Suppressed hydrogen embrittlement of high-strength Al alloys by Mn-rich intermetallic compound particles, Acta Mater. 236 (2022) 118110.
[66] Q. Meng, G.S. Frankel, Effect of Cu content on corrosion behavior of 7xxx series aluminum alloys, J. Electrochem. Soc. 151 (2004) B271.
[67] O. Beyss, U. Breuer, D. Zander, An in-depth investigation of the native oxide formed on Al-Zn-Mg-Cu alloys by XPS, XRR and ToF-SIMS, Appl. Surf. Sci. 687 (2025) 162258.
[68] N. Dimitrov, J.A. Mann, M. Vukmirovic, K. Sieradzki, Dealloying of Al2CuMg in Alkaline Media, J. Electrochem. Soc. 147 (2000) 3283.
[69] N. Birbilis, M.K. Cavanaugh, R.G. Buchheit, Electrochemical behavior and localized corrosion associated with Al7Cu2Fe particles in aluminum alloy 7075-T651, Corros. Sci. 48 (2006) 4202–4215.
[70] C.Y. Barlow, P. Nielsen, N. Hansen, Multilayer roll bonded aluminium foil: processing, microstructure and flow stress, Acta Mater. 52 (2004) 3967–3972.
[71] M. Yamaguchi, T. Tsuru, K.-i Ebihara, M. Itakura, K. Matsuda, K. Shimizu, H. Toda, Hydrogen trapping in Mg2Si and Al7FeCu2 intermetallic compounds in aluminum alloy: first-principles calculations, Mater. Trans. 61 (2020) 1907–1911.
[72] Y. Yao, R. Euesden, M.E. Curd, C. Liu, A. Garner, T.L. Burnett, P. Shanthraj, P. B. Prangnell, Effect of cooling rate on the composition and chemical heterogeneity of quench-induced grain boundary η-phase precipitates in 7xxx aluminium alloys, Acta Mater. 262 (2024) 119443.
[73] E. Lunarska, O. Chernyayeva, Effect of the self-induced strain on the hydrogen permeation through Al, Int. J. Hydrog. Energy 31 (2006) 237–246.
[74] E. Lunarska, O. Chernyayeva, Strain induced up-hill diffusion of hydrogen in Al. in: Materials science forum, Trans Tech Publ, 2006, p. 165.
[75] T. Izumi, G. Itoh, N. Itoh, Hydrogen permeation behavior in aluminum alloys, transactions-materials, Res. Soc. Jpn. 29 (2004) 1765–1768.